

Generalized Hamiltonian to describe imperfections in ion-light interaction

Ming Li,¹ Kenneth Wright,¹ Neal C. Pienti,¹ Kristin M. Beck,^{1,*} Jason H. V. Nguyen,¹ and Yunseong Nam^{1,†}

¹*IonQ, College Park, MD 20740, USA*

(Dated: September 30, 2020)

We derive a general Hamiltonian that governs the interaction between an N -ion chain and an externally controlled laser field, where the ion motion is quantized and the laser field is considered beyond the plane-wave approximation. This general form not only explicitly includes terms that are used to drive ion-ion entanglement, but also a series of unwanted terms that can lead to quantum gate infidelity. We demonstrate the power of our expressivity of the general Hamiltonian by singling out the effect of axial mode heating and confirm this experimentally. We discuss pathways forward in furthering the trapped-ion quantum computational quality, guiding hardware design decisions.

I. INTRODUCTION

Trapped ions represent a promising platform for universal quantum computation, and high-fidelity quantum gates have already been demonstrated on short chains of one or two qubits [1, 2]. However, further improvements to gate fidelity and qubit count are necessary to bridge the gap between these academic demonstrations and a commercially viable quantum computer. To this end, several pathways have been proposed and demonstrated [3–5], where ion qubits are joined and separated during the quantum operations so that gates are only performed on short chains. They however come at the cost of sparse qubit connectivity between the qubits, i.e., a direct implementation of qubit-to-qubit interaction between an arbitrary pair of qubits is impossible, a known source of overhead in performing quantum computation [6–8]. They also complicate the hardware design, making the quantum hardware more error prone.

To thus move towards a larger and high-performing trapped-ion quantum computer, investigating in detail the mechanisms by which quantum computational errors may incur due to holding a modest-sized ion chain becomes an important task. By successfully addressing the identified mechanisms, one can maximize the computational quality obtained from these scalable trapped-ion quantum computer architectures, while at the same time also providing an additional advantage in quantum circuit implementation, should the addressing offer a way to reliably perform quantum computation over a longer chain of ions that admits an all-to-all qubit connectivity [6, 9]. We aim to address this challenge by systematically expanding the light-matter interaction Hamiltonian, used to drive quantum gate operations on a trapped-ion quantum computer, in imperfections such as misalignment, defocus, and ion motion. We focus in particular on the case where a two-photon Raman transition is used to implement a quantum logic gate. Our

analytical results for the coupling of the internal qubit degrees of freedom to the quantized external motion of the ion chain accurately quantifies the role of ion-beam geometry in determining the quantum gate fidelity, in addition to the sensitivity of the fidelity with respect to ion-chain heating. We experimentally confirm the validity of our model and show compensating pulse sequences [10, 11] can decisively help boost the fidelity of trapped-ion quantum computers.

In Sec. II we introduce the governing effective Hamiltonian of a trapped-ion quantum computer, equipped with two ion-addressing Raman beams. In Sec. III we focus on the Gaussian beam, a prototypical example used widely in the trapped-ion quantum computing community, and derive a suite of expressions required for the generalized Hamiltonian. We then derive an approximate Hamiltonian from the generalized Hamiltonian using realistic parameters in Sec. IV and compare our theoretical results with the experimental results in Sec. V. We discuss our work in Sec. VI and conclude our manuscript in Sec. VII.

We note that related and similar results that mainly focus on the effect of ion motion perpendicular to the Gaussian beams used to drive quantum gates have recently been reported in [12, 13]. Our work takes a more general approach in deriving the effective interaction Hamiltonian associated with a spatially dependent light field, which enables systematic and quantitative error analysis for a variety of hardware implementations of trapped-ion based quantum computers. Our methodology further enables zooming in on individual error sources and provide guidance in devising appropriate error mitigation strategies via the expressive power offered by our generalized Hamiltonian.

II. GENERAL THEORY DERIVATION

In this section, we derive the Hamiltonian H that couples the motional degrees of freedom of the ions with their internal degrees of freedom through the spatial dependent Raman beams. This Hamiltonian can be separated into two parts as

$$H = H_0 + H_I, \quad (1)$$

* Current address: Physics Division, Physical and Life Sciences, Lawrence Livermore National Laboratory, Livermore, California 94550, USA

† nam@ionq.co

where H_0 includes the internal and the motional degrees of freedom for the ions independently and H_I describes the light-matter interaction that couples the two. Treating the laser field of the Raman beams classically, while treating the rest of the system quantum mechanically, together with the dipole approximation, H_I can simply be written as

$$H_I = - \sum_{k=1}^N \vec{E} \cdot \vec{d}_k, \quad (2)$$

where \vec{E} is the electric field and \vec{d}_k is the dipole operator of the k th ion out of N total number of ions. For H_0 we consider ions that are confined in a linear Paul trap along the potential-null line. We assume the harmonic approximation of the collective motion of the ions. Focusing now on an effective two-level system for the internal degrees of freedom of interest for each ion as a qubit, we can then write

$$H_0 = \sum_{k=1}^N \frac{\hbar\omega_k^{\text{qbt}}}{2} \hat{\sigma}_k^z + \sum_{p=1}^{3N} \hbar\omega_p \left(\hat{a}_p^\dagger \hat{a}_p + \frac{1}{2} \right), \quad (3)$$

where \hbar is the reduced Planck constant, ω_k^{qbt} is the effective qubit angular frequency for the k th ion, $\hat{\sigma}_k^\alpha$ with $\alpha = x, y, \text{ or } z$ is the Pauli matrix along the α -axis, ω_p is the normal mode frequency of the p th normal mode with Fock state creation and annihilation operators \hat{a}_p^\dagger and \hat{a}_p .

From here on, we consider only two Raman beams that drive qubit transitions on a particular ion k , and we drop the ion index wherever contextually clear for simplicity. The electric field near the ion is given by

$$\vec{E} = \vec{E}_1 + \vec{E}_2, \quad (4)$$

where the individual electric field \vec{E}_b with $b = 1$ or 2 can be written as

$$\vec{E}_b = \hat{\epsilon}_b e^{i\omega_b t} E_b(\vec{r}_b) e^{i\Phi_b(\vec{r}_b)} + \text{h.c.}, \quad (5)$$

where $\hat{\epsilon}_b$ is the polarization vector, ω_b is the angular frequency, E_b and Φ_b are real functions of the ion position in each of the beam propagation coordinates \vec{r}_b , and h.c. denotes the Hermitian conjugate. After adiabatic elimination of the excited internal states of an ion [14], we can approximate the individual summand $H_{I,k}$ of the interaction Hamiltonian H_I in (2) as

$$H_{I,k} = \bar{D} e^{i(\omega^{\text{qbt}} + \Delta\omega)t} E_1 e^{i\Phi_1} E_2 e^{-i\Phi_2} \hat{\sigma}_k + \text{h.c.}, \quad (6)$$

where \bar{D} is an effective dipole constant, $\Delta\omega$ is the effective two-photon detuning of the Raman transition from the qubit transition, and $\hat{\sigma}_k$ is a qubit spin operator which depends on the details of the Raman transition scheme. Here, without loss of generality, we assume $\omega_1 - \omega_2 = \omega^{\text{qbt}} + \Delta\omega$, in other words, the transition from qubit state $|\downarrow\rangle$ to $|\uparrow\rangle$ requires a photon absorption from beam 1 and a photon emission from beam 2.

The coupling of the beam to the motional degrees of freedom of the ion is embedded in the \vec{r}_b dependent terms in (6). To rewrite them in terms of the normal mode operators \hat{a}_p and \hat{a}_p^\dagger , we first rewrite the ion position with respect to each beam as

$$\vec{r}_b = \vec{r}_b^{(0)} + \sum_{\alpha_b} \zeta_{\alpha_b} \hat{e}_{\alpha_b}, \quad (7)$$

where $\vec{r}_b^{(0)}$ is the equilibrium position of the ion in the beam coordinate $\{x_b, y_b, z_b\}$ and \hat{e}_{α_b} is the unit vector along the direction of the axis $\alpha_b = x_b, y_b, \text{ or } z_b$. Then we can expand the terms E_b and $e^{\pm i\Phi_b}$ near $\vec{r}_b^{(0)}$ with respect to ζ_{α_b} . Lastly, we can quantize the ion motion from the equilibrium position and rewrite it in terms of the normal mode operators as

$$\hat{\zeta}_{\alpha_b} = \sum_{p=1}^{3N} \zeta_p^{(0)} \nu_p^{\alpha_b} (\hat{a}_p + \hat{a}_p^\dagger), \quad (8)$$

where $\zeta_p^{(0)} = \sqrt{\hbar/2m\omega_p}$ is the spread of the zero-point wavefunction of mode p with the mass m of the ion and $\nu_p^{\alpha_b}$ is a matrix element of the inverse of the mode vector matrix [15]. A full accounting of the ion-laser interaction can then be made by expanding the appropriate form of $E_b e^{\pm i\Phi_b}$ for a given experimental context.

III. APPLICATION TO ELLIPTICAL ASTIGMATIC GAUSSIAN BEAMS

In this section, we derive a convenient expression for the electric field that an illuminated ion sees, subject to unavoidable non-idealities that exist in a realistic ion-beam setup. Examples of non-idealities include beam misalignment and defocus with respect to the equilibrium position of the ion, unintended ion motion, etc. Specifically, in Sec. III A, we define useful notations for a Gaussian profile of a coherent beam that we then use in Sec. III B to derive a suite of series expansions that explicitly depend on the non-ideal parameters that comprise the electric field expression. In Sec. III C we briefly discuss the ways in which noise may now couple into our system then lay out a strategy to use our derived expressions for an efficient and systematic error analysis in practice.

A. Elliptical astigmatic Gaussian beam

For the remainder of this paper, we focus on a particular form of $E_b e^{\pm i\Phi_b}$ commonly used in experimental settings, an elliptical Gaussian beam with simple astigmatism [16]. The beam amplitude E_b and phase angle Φ_b can be written using the ion position $\vec{r}_b =$

$x_b \hat{e}_{x_b} + y_b \hat{e}_{y_b} + z_b \hat{e}_{z_b}$ as

$$E_b(\vec{r}_b) = \sqrt{\frac{P_b}{\pi w_{x_b} w_{z_b}}} e^{-\left(\frac{x_b^2}{w_{x_b}^2} + \frac{z_b^2}{w_{z_b}^2}\right)},$$

$$\Phi_b(\vec{r}_b) = -k_b y_b + \eta_b - \frac{k_b}{2} \left(\frac{x_b^2}{R_{x_b}} + \frac{z_b^2}{R_{z_b}} \right) + \phi_b, \quad (9)$$

where we assume the beam propagates along the y_b -axis and the two principal axes are along the x_b - and the z_b -axes. Here, P_b is the power of the beam, $k_b = 2\pi/\lambda_b$ is the wavevector with λ_b the wavelength, and ϕ_b is a constant phase at the origin which can be chosen arbitrarily along the y_b -axis. w_{x_b} and w_{z_b} are the two principal semi axes of the spot ellipse at y_b , defined according to

$$w_{\alpha_b}(y_b) = w_{\alpha_b}^f \sqrt{1 + \left(\frac{y_b - y_{\alpha_b}^f}{y_{\alpha_b}^R} \right)^2}, \quad (10)$$

where $w_{\alpha_b}^f$ is the beam waist along the α_b -axis at the focal point $y_{\alpha_b}^f$ and $y_{\alpha_b}^R$ is the Rayleigh range given by $\pi(w_{\alpha_b}^f)^2/\lambda_b$. The radii of curvature R_{α_b} are given by

$$R_{\alpha_b}(y_b) = \frac{(y_b - y_{\alpha_b}^f)^2 + y_{\alpha_b}^R{}^2}{y_b - y_{\alpha_b}^f}. \quad (11)$$

η_b is the Gouy phase, i.e.,

$$\eta_b(y_b) = \frac{1}{2} \left(\arctan \frac{y_b - y_{x_b}^f}{y_{x_b}^R} + \arctan \frac{y_b - y_{z_b}^f}{y_{z_b}^R} \right). \quad (12)$$

B. Expansion of the electric field

The spatially dependent terms $E_b e^{\pm i\Phi_b}$ can be expanded from the focal points of the beam. Denoting the ion equilibrium position as $\vec{r}_b^{(0)} = x_b^{(0)} \hat{e}_{x_b} + y_b^{(0)} \hat{e}_{y_b} + z_b^{(0)} \hat{e}_{z_b}$ and the ion excursion as $\{\zeta_{x_b}, \zeta_{y_b}, \zeta_{z_b}\}$, we define the y -distance between the ion equilibrium position and the x and z focal points as $y_b^{(0)f} \equiv y_b^{(0)} - y_{\alpha_b}^f$. Then, the regime we consider here, i.e., the ion does not venture outside of the Rayleigh range from each focal point of the corresponding principal axis, may be succinctly written as $|y_b^{(0)f}| \ll y_{\alpha_b}^R$. In this regime, expanding E_b and $e^{i\Phi_b}$ in (9) about the focal points of the two principal axes $y_{x_b}^f$ and $y_{z_b}^f$, together with (10), (11), and (12), we obtain

$$E_b \equiv \sqrt{\frac{P_b}{\pi w_{x_b}^f w_{z_b}^f}} A_1(\lambda_{x_b}^{(0)}, \hat{\lambda}_{x_b}) A_1(\lambda_{z_b}^{(0)}, \hat{\lambda}_{z_b})$$

$$A_2(\lambda_{x_b}^{(0)}, \hat{\lambda}_{x_b}, \gamma_{x_b}^{(0)}, \hat{\gamma}_{x_b}) A_2(\lambda_{z_b}^{(0)}, \hat{\lambda}_{z_b}, \gamma_{z_b}^{(0)}, \hat{\gamma}_{z_b}) \quad (13)$$

and

$$e^{\pm i\Phi_b} \equiv e^{\pm i(\phi_b - k_b y_b^{(0)})} B_0^\pm(\hat{\beta}_b) B_1^\pm(\lambda_{x_b}^{(0)}, \hat{\lambda}_{x_b}) B_1^\pm(\lambda_{z_b}^{(0)}, \hat{\lambda}_{z_b})$$

$$B_2^\pm(\lambda_{x_b}^{(0)}, \hat{\lambda}_{x_b}, \gamma_{x_b}^{(0)}, \hat{\gamma}_{x_b}) B_2^\pm(\lambda_{z_b}^{(0)}, \hat{\lambda}_{z_b}, \gamma_{z_b}^{(0)}, \hat{\gamma}_{z_b}), \quad (14)$$

where we split the spatial dependent terms into the A and B functions, defined according to

$$A_1(p_0, \hat{p}_1) = [1 + (p_0 + \hat{p}_1)^2]^{-1/4} = \sum_{l_p=0}^{\infty} \hat{p}_1^{l_p} \sum_{n=\lceil l_p/2 \rceil}^{\infty} (-1)^n \frac{(4n-3)!!!!}{(4n)!!!!} \binom{2n}{l_p} p_0^{2n-l_p},$$

$$A_2(p_0, \hat{p}_1, q_0, \hat{q}_1) = \exp \left[-\frac{(q_0 + \hat{q}_1)^2}{1 + (p_0 + \hat{p}_1)^2} \right]$$

$$= \sum_{l_q, l_p=0}^{\infty} \hat{q}_1^{l_q} \hat{p}_1^{l_p} \sum_{\substack{n=\lceil l_q/2 \rceil \\ m=\lceil l_p/2 \rceil}}^{\infty} \frac{(-1)^{n+m}}{n!} \binom{n+m-1}{m} \binom{2n}{l_q} \binom{2m}{l_p} q_0^{2n-l_q} p_0^{2m-l_p},$$

$$B_0^\pm(\hat{p}_1) = e^{\mp i\hat{p}_1} = \sum_{n=0}^{\infty} \frac{(\mp i)^n}{n!} \hat{p}_1^n,$$

$$B_1^\pm(p_0, \hat{p}_1) = \exp \left[\frac{\pm i}{2} \arctan(p_0 + \hat{p}_1) \right] = \sum_{n=0}^{\infty} \frac{(\pm i)^n}{2^n n!} \left\{ \sum_{l_p=0}^{\infty} \hat{p}_1^{l_p} \sum_{m=\lceil (l_p-1)/2 \rceil}^{\infty} \frac{(-1)^m}{2m+1} \binom{2m+1}{l_p} p_0^{2m+1-l_p} \right\}^n,$$

$$B_2^\pm(p_0, \hat{p}_1, q_0, \hat{q}_1) = \exp \left[\mp i \frac{(p_0 + \hat{p}_1)(q_0 + \hat{q}_1)^2}{1 + (p_0 + \hat{p}_1)^2} \right]$$

$$= \sum_{l_q, l_p=0}^{\infty} \hat{q}_1^{l_q} \hat{p}_1^{l_p} \sum_{\substack{n=\lceil l_q/2 \rceil \\ m=\lceil l_p/2 \rceil}}^{\infty} \frac{(\mp i)^n (-1)^m}{n!} \binom{n+m-1}{m} \binom{2n}{l_q} \binom{2m}{l_p} (p_0 + \hat{p}_1)^n q_0^{2n-l_q} p_0^{2m-l_p}, \quad (15)$$

where (\cdot) denotes a binomial coefficient, $\lceil \cdot \rceil$ denotes the ceiling function, p_0 may be $\lambda_{x_b}^{(0)}$ or $\lambda_{z_b}^{(0)}$, \hat{p}_1 may be $\hat{\lambda}_{x_b}$, $\hat{\lambda}_{z_b}$, or $\hat{\beta}_b$, q_0 may be $\gamma_{x_b}^{(0)}$ or $\gamma_{z_b}^{(0)}$, \hat{q}_1 may be $\hat{\gamma}_{x_b}$ or $\hat{\gamma}_{z_b}$, and

$$\begin{aligned}\hat{\beta}_b &= k_b \hat{\zeta}_{y_b} = \sum_p c_{p,y_b}^\beta (\hat{a}_p + \hat{a}_p^\dagger), \\ \gamma_{x_b}^{(0)} &= \frac{x_b^{(0)}}{w_{x_b}^f}, \quad \hat{\gamma}_{x_b} = \frac{\hat{\zeta}_{x_b}}{w_{x_b}^f} = \sum_p c_{p,x_b}^\gamma (\hat{a}_p + \hat{a}_p^\dagger), \\ \gamma_{z_b}^{(0)} &= \frac{z_b^{(0)}}{w_{z_b}^f}, \quad \hat{\gamma}_{z_b} = \frac{\hat{\zeta}_{z_b}}{w_{z_b}^f} = \sum_p c_{p,z_b}^\gamma (\hat{a}_p + \hat{a}_p^\dagger), \\ \lambda_{x_b}^{(0)} &= \frac{y_{x_b}^{(0)f}}{y_{x_b}^R}, \quad \hat{\lambda}_{x_b} = \frac{\hat{\zeta}_{y_b}}{y_{x_b}^R} = \sum_p c_{p,x_b}^\lambda (\hat{a}_p + \hat{a}_p^\dagger), \\ \lambda_{z_b}^{(0)} &= \frac{y_{z_b}^{(0)f}}{y_{z_b}^R}, \quad \hat{\lambda}_{z_b} = \frac{\hat{\zeta}_{y_b}}{y_{z_b}^R} = \sum_p c_{p,z_b}^\lambda (\hat{a}_p + \hat{a}_p^\dagger)\end{aligned}\quad (16)$$

are dimensionless. We quantize β_b , γ_{α_b} , and λ_{α_b} and use Eq. (8) to express the A and B functions defined in (15) in terms of normal mode ladder operators and collect all the non-operator coefficients into the c -coefficients. Note that the c -coefficients are inversely proportional to the square-root of their corresponding mode frequencies. Further note that the B_0^\pm terms are conventionally used to formulate two-qubit entangling gates, for instance the Mølmer-Sørensen protocol [17, 18] or the Cirac-Zoller protocol [19]. It is sometimes easier to maintain the exponential form for B_0^\pm since its exponent only has first order terms of ladder operators.

We briefly emphasize that the Hamiltonian framework detailed in this section is entirely general. It enables quantum hardware designers to straightforwardly assess the impact of a variety of experimental imperfections on the quantum computational fidelity. Our framework serves as a diagnostic tool that aids the designers locate the major sources of quantum computational errors, critical for developing powerful quantum computers.

C. Error channels and analysis strategy

By examining the expansions reported above, one can identify four general mechanisms by which a quantum computational error can occur through the spatially dependent terms. Firstly, any misalignment, defocus, or distortion of a Raman beam that is not accounted for can lead to quantum computational errors. Secondly, when there is stray field near the ion that are not compensated or accounted for, errors may also arise. In these two situations, errors propagate through all of the parameters in (16). Specifically, they affect the scaled-position parameters $\gamma_{\alpha_b}^{(0)}$, $\lambda_{\alpha_b}^{(0)}$, or the non-operator terms in the definition of $\hat{\beta}_b$, $\hat{\gamma}_{\alpha_b}$, or $\hat{\lambda}_{\alpha_b}$, *i.e.* the zero-point spread $\zeta_p^{(0)}$, the matrix element $\nu_p^{\alpha_b}$ of the inverse mode vector

matrix, the beam waist $w_{\alpha_b}^f$, or the Rayleigh range $y_{R_{\alpha_b}}$. Thirdly, an error can occur through the so-called resonant terms that do not change the motional space, *i.e.* they have equal numbers of \hat{a}_p and \hat{a}_p^\dagger operators. Any even total power of $\hat{\beta}_b$, $\hat{\gamma}_{\alpha_b}$, and/or $\hat{\lambda}_{\alpha_b}$ would contain resonant terms. Apart from the trivial case of a constant term, all the other terms depend on the occupation of the motional Fock space. Thus any imprecise control or erroneous information on the motional space can lead to quantum computational errors in the manipulation of ion qubits. A classic example of this mechanism is the well-known Debye-Waller effect [20]. Lastly, the rest of the \hat{a}_p and \hat{a}_p^\dagger dependent terms lead to an excursion in the phase space of the ion during a quantum gate operation. When such an excursion occurs and the ion is not returned to its initial position in the phase space after the completion of the gate operation, it can lead to unwanted, lingering entanglement between the qubit space and the motional space, which are nontrivial to correct for. This effect could in part be suppressed by reducing the corresponding coefficient for the \hat{a}_p and \hat{a}_p^\dagger dependent terms, sufficient detunings from any motional sideband resonances, or by actively shaping the gate pulse [21].

In practice, it is cumbersome to directly use the expressions of A and B functions in (15). A proper and justifiable truncation of the power series in (15) becomes an important task for an approximate yet effective error analysis. We observe that each function in (15) can be written in the form of a summation of operators, $\sum_{ij} \hat{O}_{ij}$, where each operator is in the form of $c_{ij} \hat{p}_1^i \hat{q}_1^j$. c_{ij} here is a complex constant and c_{00} is always non-zero. Our task then boils down to neglecting some of the operators if their contribution to the Hamiltonian is small. To quantify the contribution, we use the operator norm $\|\hat{O}_{ij}\|$. We evaluate the norm in a large but finite motional space, truncated such that realistic motional-space dynamics can be adequately captured within. In the next section, we will perform the error analysis for a realistic situation and provide a concrete example.

We note in passing that we can rewrite the power series of the non-operator terms in (15) in a more compact way by examining terms with ascending power of \hat{p}_1 . Doing so renders evaluating the size of the individual coefficients of the powers of \hat{p}_1 more straightforward. We report the results for the first three orders in Appendix A for the convenience of the readers.

IV. PARALLEL RAMAN BEAM GEOMETRY

In this section, we provide a concrete analysis based on (15) for a realistic set of Raman beam parameters relevant to contemporary trapped-ion quantum computing architectures with parallel Raman beams configured to be either co- or counter-propagating. In Sec. IV A we specify sizes of the parameters commensurate to a contemporary trapped-ion quantum computer. In Sec. IV B,

we follow through the error analysis strategy laid out in Sec. III C and present a simplified version of the evolution operator that approximately describes the quantum state evolution. In Sec. IV C, we subject our approximate evolution operator to application and show in particular the significance of the axial mode temperature in determining quantum gate fidelity when using tightly focused Raman beams.

We emphasize that, intuitively speaking, the impact on quantum gate fidelity due excessive axial mode temperature is similar to that due to the Debye-Waller effect, *i.e.* the Rabi frequency for driving the spin degree of freedom depends on the phonon number of the axial motional state. Therefore, any distribution of motional state with a non-zero width directly translates to a distribution in the Rabi frequency with a corresponding non-zero width that decoheres the quantum gate operation. We briefly re-discuss this point towards the end of Sec. IV C once we derive all necessary expressions for computing the quantum gate fidelity.

A. Parameter specifications

We assume a linear chain of ions, addressed by an array of Raman beams propagating in parallel, capable of driving transitions between $|\downarrow\rangle$ and $|\uparrow\rangle$, tightly focused along the chain axis, to achieve individual addressability of qubits along the chain. We refer to the normal modes of the ion chain depending on the dominant projection of their mode vector – axial modes are predominantly along \hat{x}_b , horizontal modes along \hat{y}_b , and vertical modes along \hat{z}_b . Our coordinate systems are defined with respect to the axes of the Raman beams, which are assumed to propagate along \hat{y}_b transverse to the chain axis, and exhibit an elliptical Gaussian profile with the loose (tight) dimension along \hat{z}_b (\hat{x}_b). The equilibrium position of each ion is assumed to reside near the focal point of each Raman beam, such that we satisfy $\gamma_{\alpha_b}^{(0)}, \lambda_{\alpha_b}^{(0)} \ll 1$

For a quantitative analysis, we consider Raman beams with a wavelength $\lambda = 355$ nm and a waist $w_{x_b}^f$ ($w_{z_b}^f$) larger or similar to ~ 1 μm (~ 5 μm), as might be found on a $^{171}\text{Yb}^+$ trapped ion quantum computer. The corresponding Rayleigh range $y_{R_{x_b}}$ ($y_{R_{z_b}}$) is then larger or similar to ~ 10 μm (~ 200 μm). We assume the alignment errors in $|x_b^{(0)}|$ and $|z_b^{(0)}|$ are less than 100 nm, and the focusing error in $|y_{\alpha_b}^{(0)f}|$ is bounded by 10% of the corresponding Rayleigh range. Then, we have $|\gamma_{x_b}^{(0)}| < 0.1$, $|\gamma_{z_b}^{(0)}| < 0.02$, $|\lambda_{x_b}^{(0)}| < 0.1$, and $|\lambda_{z_b}^{(0)}| < 0.1$. Similarly, we quantify the alignment of a given normal mode to the dominant principle axes of the Raman beams by an error parameter ε , defined as the size of the maximal relative excursion of the mode vector matrix elements $\nu_p^{\alpha b}$ in non-dominant principle axis directions scaled by a factor of \sqrt{N} . The magnitude of unintended projection of each mode vector along $\{\hat{x}, \hat{y}, \hat{z}\}$ are then bounded as given in Table I. For the system we consider, we assume ε to be

TABLE I. Alignment of the principal axes of the Gaussian beams with the mode vectors of different sets of modes.

	Axial modes	Horizontal modes	Vertical modes
$ \nu_p^{x_b} $	$\sim 1/\sqrt{N}$	$< \varepsilon/\sqrt{N}$	$< \varepsilon/\sqrt{N}$
$ \nu_p^{y_b} $	$< \varepsilon/\sqrt{N}$	$\sim 1/\sqrt{N}$	$< \varepsilon/\sqrt{N}$
$ \nu_p^{z_b} $	$< \varepsilon/\sqrt{N}$	$< \varepsilon/\sqrt{N}$	$\sim 1/\sqrt{N}$

smaller than 0.05. Normal mode frequencies $\omega_p/2\pi$ are taken to be approximately 3 MHz horizontally, 2.5 MHz vertically, and depending on the number of ions, chain spacing, and the DC potential, anywhere from 150 kHz to ~ 2 MHz axially. The resulting magnitude of the c -coefficients that appear in (16) are summarized in Table II.

We utilize Doppler cooling on the $^2S_{1/2}$ to $^2P_{1/2}$ transition to cool the Yb^+ ions. The mode temperatures after the Doppler cooling are given by the average phonon number at the Doppler limit $\bar{n}_p^D = \Gamma/2\omega_p$ where $\Gamma = 2\pi \times 19.6$ MHz is the natural linewidth of the excited $^2P_{1/2}$ state. Thus the average phonon number at the Doppler limit is ~ 4 quanta for the non-axial modes, and can range from ~ 5 to ~ 70 quanta for the axial modes depending on the mode frequencies. For the horizontal modes, in the case of counter-propagating set up, we apply a sideband cooling sequence, which consists of coherent red sideband pulses, followed by optical pumping. This consistently cools the horizontal modes to $\bar{n} \lesssim 0.1$.

B. Hamiltonian approximation

Equipped with the realistic parameter values detailed above, we now proceed with the power-series truncation strategy laid out in Sec. III C. To do so, we need to first determine the extent of truncation in the motional Hilbert space. As a guiding principle, we would like to include a large enough motional space for a specific mode so that for a thermal state considered in that mode the population distributed outside of the truncated motional space accounts for less than 10^{-3} . For the non-axial directions, we base this off of the initial temperature of our ion crystal, which is the Doppler temperature [22], since the crystal does not easily heat in these directions. For the axial, the modes readily heat, and we are interested in the fidelity impact from excessive axial mode temperature after a time period of heating. This motivates us to consider $\sim 10^2$ quanta for the non-axial and $\sim 10^4$ quanta for the axial cutoffs for the three directions, assuming e.g., each and every mode for a given direction heat more or less evenly. Note however that it is possible that there could be a dominant mode per direction that heats the most while the rest of the modes do not readily heat. To account for such a case, we also consider $\sim 10^2 \times N$ quanta for the dominant non-axial and $\sim 10^4 \times N$ quanta for the dominant axial modes. When

TABLE II. Estimates of the magnitude of the c -coefficients in Eq. (16) using the realistic experimental parameters and conditions detailed in the main text of Sec. IV.

$\omega_p/2\pi$	Axial modes			Horizontal modes		Vertical modes
	150 kHz	600 kHz	2.0 MHz	3.0 MHz	2.5 MHz	
$ c_{p,y_b}^\beta \times \sqrt{N}$	$\lesssim 1\text{e-}2$	$\lesssim 6\text{e-}3$	$\lesssim 3\text{e-}3$	$\lesssim 6\text{e-}2$	$\lesssim 3\text{e-}3$	
$ c_{p,x_b}^\gamma \times \sqrt{N}$	$\lesssim 1\text{e-}2$	$\lesssim 7\text{e-}3$	$\lesssim 4\text{e-}3$	$\lesssim 2\text{e-}4$	$\lesssim 2\text{e-}4$	
$ c_{p,z_b}^\gamma \times \sqrt{N}$	$\lesssim 1\text{e-}4$	$\lesssim 7\text{e-}5$	$\lesssim 4\text{e-}5$	$\lesssim 3\text{e-}5$	$\lesssim 7\text{e-}4$	
$ c_{p,x_b}^\lambda \times \sqrt{N}$	$\lesssim 7\text{e-}5$	$\lesssim 4\text{e-}5$	$\lesssim 2\text{e-}5$	$\lesssim 3\text{e-}4$	$\lesssim 2\text{e-}5$	
$ c_{p,z_b}^\lambda \times \sqrt{N}$	$\lesssim 4\text{e-}6$	$\lesssim 2\text{e-}6$	$\lesssim 1\text{e-}6$	$\lesssim 2\text{e-}5$	$\lesssim 9\text{e-}7$	

determining which operator terms \hat{O}_{ij} to drop from our Hamiltonian, we consider both cases, i.e., even heating of all modes and concentrated heating of a dominant mode for each direction. We drop \hat{O}_{ij} from the Hamiltonian in devising the effective Hamiltonian, only if the fractional contribution from \hat{O} is less than 10^{-2} in both cases. We assume $N \leq 50$ for concreteness.

The expressions in (15) (see Appendix A, Eq. (A1) for the ordered form) may now be approximated according to the strategy outlined in Sec. III C with the parameters specified in Sec. IV A. Keeping only the terms with the size of the fractional contribution larger than 10^{-2} , we obtain

$$\begin{aligned}
A_1 &\approx s_0^{1/2}, \\
A_2 &\approx e^{-s_0^2 q_0^2} \sum_{l_q=0}^{\infty} \frac{(-s_0 \hat{q}_1)^{l_q}}{l_q!} \mathcal{H}_{l_q}(s_0 q_0) \\
&= \exp[-s_0^2 (q_0 + \hat{q}_1)^2] \\
B_0^\pm &= e^{\mp i \hat{p}_1}, \\
B_1^\pm &\approx e^{\pm \frac{1}{2} \arctan(p_0)}, \\
B_2^\pm &\approx e^{\mp i s_0^2 q_0^2 p_0}, \tag{17}
\end{aligned}$$

where $s_0 = 1/\sqrt{1+p_0^2}$. Note we may further approximate the the A_2 function in (17) in the case where it is used for z_b direction, as in the second A_2 function used in (13). Specifically, $A_2(\lambda_{z_b}^{(0)}, \hat{\lambda}_{z_b}, \gamma_{z_b}^{(0)}, \hat{\gamma}_{z_b})$ function may be truncated to $\exp(-\gamma_{z_b}^{(0)2}/(1+\lambda_{z_b}^{(0)2}))$, due to the larger beam waist and lower vertical mode temperature along the z_b directions. We assumed here $q_0 = \gamma_{z_b}^{(0)}$ and $\hat{q}_1 = \hat{\gamma}_{z_b}$.

Inserting the simplified A and B functions to the amplitude and phase functions in (13) and (14), respectively, then inserting the simplified amplitude and phase functions to the interaction Hamiltonian in (6), we obtain

$$H_I = \hbar \Omega_0 \sum_{l=0}^{\infty} \sum_{m=0}^l \frac{(-1)^l}{m!(l-m)!} \hat{\gamma}_{\lambda,x_1}^m \hat{\gamma}_{\lambda,x_2}^{l-m} \mathcal{H}_m(\gamma_{\lambda,x_1}^{(0)}) \mathcal{H}_{l-m}(\gamma_{\lambda,x_2}^{(0)}) \left[e^{i[(\omega^{\text{qbt}} + \Delta\omega)t + \Psi_0]} \hat{\sigma} + \text{h.c.} \right], \tag{18}$$

with $\hat{\gamma}_{\lambda,x_b} = \hat{\gamma}_{x_b}/\sqrt{1+\lambda_{x_b}^{(0)2}}$ and $\gamma_{\lambda,x_b}^{(0)} = \gamma_{x_b}^{(0)}/\sqrt{1+\lambda_{x_b}^{(0)2}}$. We collected all non-operator terms into a Rabi rate term

Ω_0 and a phase term Ψ_0 , defined as

$$\begin{aligned}
\Omega_0 &= \frac{\bar{D}}{\pi \hbar} \sqrt{\frac{P_1 P_2}{w_{x_1}^f w_{x_2}^f w_{z_1}^f w_{z_2}^f}} \\
&\left[(1 + \lambda_{x_1}^{(0)2})(1 + \lambda_{x_2}^{(0)2})(1 + \lambda_{z_1}^{(0)2})(1 + \lambda_{z_2}^{(0)2}) \right]^{-1/4} \\
&\exp \left[-\frac{\gamma_{x_1}^{(0)2}}{1 + \lambda_{x_1}^{(0)2}} - \frac{\gamma_{x_2}^{(0)2}}{1 + \lambda_{x_2}^{(0)2}} - \frac{\gamma_{z_1}^{(0)2}}{1 + \lambda_{z_1}^{(0)2}} - \frac{\gamma_{z_2}^{(0)2}}{1 + \lambda_{z_2}^{(0)2}} \right] \tag{19}
\end{aligned}$$

and

$$\begin{aligned} \Psi_0 &= \phi_1 - \phi_2 + k_2 y_{x_2}^{(0)} - k_1 y_{x_1}^{(0)} \\ &+ \frac{1}{2} \left[\arctan \lambda_{x_1}^{(0)} + \arctan \lambda_{x_2}^{(0)} + \arctan \lambda_{z_1}^{(0)} + \arctan \lambda_{z_2}^{(0)} \right] \\ &- \left[\frac{\lambda_{x_1}^{(0)} \gamma_{x_1}^{(0)2}}{1 + \lambda_{x_1}^{(0)2}} + \frac{\lambda_{x_2}^{(0)} \gamma_{x_2}^{(0)2}}{1 + \lambda_{x_2}^{(0)2}} + \frac{\lambda_{z_1}^{(0)} \gamma_{z_1}^{(0)2}}{1 + \lambda_{z_1}^{(0)2}} + \frac{\lambda_{z_2}^{(0)} \gamma_{z_2}^{(0)2}}{1 + \lambda_{z_2}^{(0)2}} \right]. \end{aligned} \quad (20)$$

To arrive at (18), we used $\|e^{i(\hat{\beta}_2 - \hat{\beta}_1)} - 1\| \approx 1$ for both the co- and counter-propagating beams, which means that the Debye-Waller effect [20] is negligible. In the co-propagating set up, the local coordinate systems of the beams are mostly aligned and when the two B_0^\pm functions are substituted into the Hamiltonian, the resulting term $e^{i(\hat{\beta}_2 - \hat{\beta}_1)}$ becomes very close to an identity operation due to the cancellation of the $\hat{\beta}_b$ operators. More specifically, using the information of the system given previously, it is straightforward to show that $\|e^{i(\hat{\beta}_2 - \hat{\beta}_1)} - 1\|$ is smaller than 10^{-2} . In the counter-propagating set up, $e^{i(\hat{\beta}_2 - \hat{\beta}_1)} - 1$ does contribute significantly to the Hamiltonian, unless the horizontal modes are sufficiently cooled so that $n_H \ll 1$. Since we cool the horizontal modes using sideband cooling to suppress the Debye-Waller effect in all experiments that use the counter-propagating set up, $\|e^{i(\hat{\beta}_2 - \hat{\beta}_1)} - 1\|$ may be assumed smaller than 10^{-2} and can thus be neglected, like in the co-propagating case.

The interaction Hamiltonian in (18) can readily be

$$H_I = \hbar\Omega_0 \sum_{l=0}^{\infty} \frac{(-1)^l}{l!} (\eta)^l \mathcal{H}_l(\xi) (e^{-i\omega t} \hat{a} + e^{i\omega t} \hat{a}^\dagger)^l \left[e^{i(\Delta\omega t + \Psi_0)} \hat{\sigma} + \text{h.c.} \right], \quad (21)$$

where

$$\begin{aligned} \eta &= \frac{\zeta^{(0)} \nu^x}{w_x^{\text{eff}} \sqrt{1 + y_x^{(0)f2} / y_x^{\text{R}2}}}, \\ \xi &= \frac{x^{(0)}}{w_x^{\text{eff}} \sqrt{1 + y_x^{(0)f2} / y_x^{\text{R}2}}}. \end{aligned} \quad (22)$$

w_x^{eff} is the effective waist given by $w_x^f / \sqrt{2}$.

In the second situation, which is representative of the counter-propagating set up, we have one of the Raman beams to be narrowly focused and individually addressing while the other to be very loosely focused and capable of addressing a long ion chain. The loosely focused, global addressing beam has a waist of more than $100 \mu\text{m}$ which allows us to truncate any $\hat{\gamma}_{\lambda,x}^m$ term with $m > 0$. Thus, the interaction Hamiltonian is again of the form in

used to assess fidelity impacts of noise sources ranging from beam misalignment and instability, to noise on the ion positions, as well as excessive mode temperature in a single-qubit gate operation using, for instance, a Monte-Carlo type simulation. It can also be easily incorporated into a two-qubit Hamiltonian to evaluate errors in a two-qubit gate operation. Note that when the two beams are perfectly aligned with each other, Eq. (18) reduces to a single summation with only one Hermite polynomial term in each summand, which reproduces the results given in Ref. [13].

C. Axial mode temperature effect

Here, we put our Hamiltonian expression in (18) to test by investigating the fidelity impact of excessive axial mode temperature. We assume that only one axial mode, for instance the center-of-mass (COM) mode, has a dominant behavior in determining the temperature, thus dropping the mode index p . Next, we consider two realistic situations regarding the beam waist and the beam alignment.

In the first situation, which is representative of the co-propagating set up, we have two tightly focused beams with identical waists $w_{x_1}^f = w_{x_2}^f$. As a good approximation, we can assume that they are perfectly aligned, *i.e.* $\gamma_{\lambda,x_1}^{(0)} = \gamma_{\lambda,x_2}^{(0)}$ and $|c_{p,x_1}^\gamma| = |c_{p,x_2}^\gamma|$. Then the summation of m in (18) reduces to a single term due to a sum rule of products of two Hermite polynomials. We can then transform the interaction Hamiltonian with $U_0 = \exp(-iH_0 t / \hbar)$ and obtain

(21). The only difference is that the effective waist here is given by waist w_x^f of the narrowly focused beam.

For a single-qubit gate operation, we drive the Raman transition at the qubit frequency, *i.e.* $\Delta\omega = 0$. Then any term with imbalanced numbers of \hat{a} and \hat{a}^\dagger are off-resonant and thus suppressed [23]. Neglecting these fast-rotating couplings, we can simply write the evolution operator of a single-qubit gate pulse that has a constant power of a time duration of t_{sqg} as

$$U_I = e^{-iH_I t_{\text{sqg}} / \hbar} \approx \sum_n \left(\cos \Theta_n \hat{I} - i \sin \Theta_n \hat{\sigma}_{\Psi_0} \right) |n\rangle \langle n|, \quad (23)$$

where $|n\rangle$ is a Fock state in the axial mode space, $\hat{\sigma}_{\Psi_0} = \exp(i\Psi_0) \hat{\sigma} + \text{h.c.}$, \hat{I} is the identity operator in the qubit

space, and Θ_n is defined as

$$\Theta_n = \Omega_0 t_{\text{sqg}} \sum_{m=0}^{\infty} \left(\frac{-\eta^2}{2} \right)^m \frac{\mathcal{H}_{2m}(\xi)}{m!} {}_2\mathcal{F}_1(1+n, -m; 1; 2). \quad (24)$$

Here we used

$$\begin{aligned} \langle n | (\hat{a} + \hat{a}^\dagger)^{2m} | n \rangle &= \sum_{i=0}^m \left(-\frac{1}{2} \right)^{m-i} \frac{(n+i)! (2m)!}{n! (m-i)! (i!)^2} \\ &= \left(-\frac{1}{2} \right)^m \frac{(2m)!}{m!} {}_2\mathcal{F}_1(1+n, -m; 1; 2), \end{aligned} \quad (25)$$

where ${}_2\mathcal{F}_1(a, b; c; z)$ denotes a Gaussian hypergeometric function. Equation (24) explicitly shows how the Rabi frequency for driving the spin degree of freedom depends on the phonon occupation of the axial motional state. Thus a distribution of the phonon occupation number of the axial motional state with a non-zero width results in a distribution of the Rabi frequency with a corresponding non-zero width which in turn induces decoherence to the quantum gate operation.

Note that the convergence of (24) greatly depends on η and n . For instance, for perfect alignment, *i.e.* $\xi \rightarrow 0$, with $\eta = 0.01$ and $n = 2000$, we need $m = 4$ to achieve convergence to the third significant digit. To achieve the same accuracy, we need $m = 11$ for $\eta = 0.02$ and $n = 2000$, and $m = 92$ for $\eta = 0.02$ and $n = 20000$. To mitigate some of the convergence issue, if we assume $\xi \rightarrow 0$, we have $\mathcal{H}_{2m} = (-1)^m (2m)!/m!$, and we can simplify (24) to

$$\Theta_n = \frac{\Omega_0 t_{\text{sqg}}}{\sqrt{1+2\eta^2}} {}_2\mathcal{F}_1\left(\frac{1}{2}, -n; 1; \frac{4\eta^2}{1+2\eta^2}\right). \quad (26)$$

Once proper care for convergence is taken, it is straightforward to insert (26) in (23) to evaluate the effect of the axial mode temperature on the fidelity of a single-qubit gate operation for different initial states and measurement schemes. We carry out such an analysis in more detail in the next section in conjunction with our experimental results.

V. EXPERIMENT

In this section, we experimentally investigate the impact of high-temperature axial modes in the presence of tightly focused Raman laser beams. A similar experimental apparatus has been discussed in detail elsewhere [24], but we briefly discuss the key features here for completeness. We load a chain of $^{171}\text{Yb}^+$ ions in a surface-electrode ion trap, where we can control the axial chain spacing by adjusting the voltages on several DC electrodes on the trap. Quantum logic gates are performed via Raman transitions induced by two 355 nm Gaussian beams. The state initialization follows a Doppler cooling sequence, where the initial motional temperature is

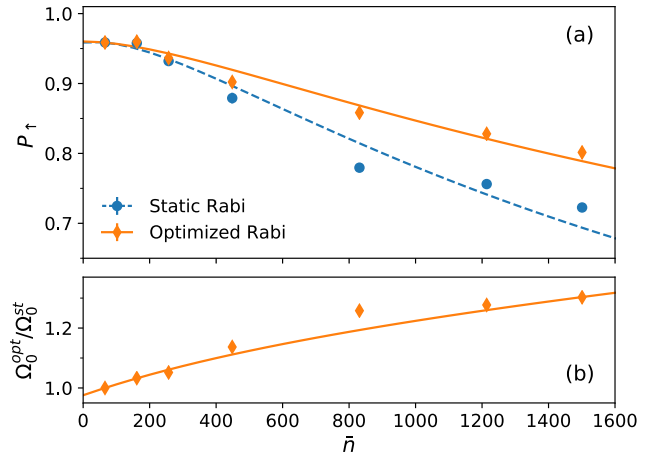


FIG. 1. Implementation of the delayed gate protocol (A)-(D) detailed in the main text. A single ion with axial frequency $\omega_A = 2\pi \times 153$ kHz was used in a co-propagating set up. (a) P_\uparrow as a function of \bar{n} . Experimental (points) and simulation (lines) results show the optimized Rabi approach (orange diamonds and solid line) can mitigate the P_\uparrow decay induced by the mode heating, shown here by the static approach result (blue circles and dashed line). (b) the ratio $\Omega_0^{\text{opt}}/\Omega_0^{\text{st}}$ as a function of \bar{n} . The orange diamonds are the experimental results and the orange solid line is the theoretical simulation results. See Sec. VC for model details.

cooled to the Doppler limit. When using the counter-propagating set up, the horizontal modes are further cooled to $\bar{n} \lesssim 0.1$ using a sideband cooling sequence. This reduces to the effective Hamiltonian of Eq. (3), where our qubit states $\{|\downarrow\rangle, |\uparrow\rangle\}$ are taken to be the $|F=0, m_F=0\rangle$ and $|F=1, m_F=0\rangle$ hyperfine levels of the ground electronic state, respectively. High-fidelity state preparation is done via optical pumping to the $|\downarrow\rangle$ at the beginning of each experiment, and measurement is done by spatially resolved, state-dependent fluorescence detection [25].

A. Measurement of axial mode temperature effect

Following the theoretical analysis shown in Sec. IV, we experimentally probe the following steps specifically: (A) we initialize our quantum state to $\rho_0(0) = |\downarrow\rangle\langle\downarrow| \otimes \rho_T(0)$, where $|\downarrow\rangle$ is a qubit state vector and

$$\rho_T(t) = \sum_n \frac{\bar{n}_t^n}{(1+\bar{n}_t)^{n+1}} |n\rangle\langle n| \quad (27)$$

is the density operator of a thermal state of the axial mode at time t with an average Fock state occupation number \bar{n}_t ; (B) we wait for time Δt so that the axial motional state is heated to a higher $\bar{n}_{\Delta t}$ and the quantum state becomes $\rho_0(\Delta t)$; (C) we implement a single-qubit gate whose unitary is given by (23) with $\hat{\sigma}_{\Psi_0} = \hat{\sigma}_x$; (D) we measure the final state and repeat the experiment to

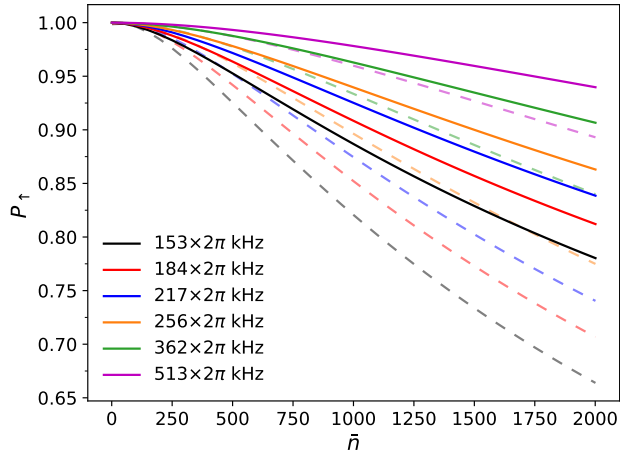


FIG. 2. Theoretical simulations of P_{\uparrow} as a function of \bar{n} for single ion in a co-propagating set up. Results for six different axial mode frequencies are presented. The solid lines represent the optimized Rabi approach and the dashed lines represent the static Rabi approach. For each line style, the color coded lines from top to bottom correspond to having axial mode frequencies from high to low as listed in the legend.

sample the probability of the final state being measured in $|\uparrow\rangle$. Denoting the measurement projector as $M = |\uparrow\rangle\langle\uparrow| \otimes \hat{I}_{\text{mot}}$, where \hat{I}_{mot} is the identity operator in the motional space, based on Sec. IV C, the probability to measure a positive measurement outcome P_{\uparrow} is given by

$$P_{\uparrow}(\bar{n}_{\Delta t}) = \text{Tr}[U_I \rho_0(\Delta t) U_I^\dagger M] \\ = \sum_n \frac{\bar{n}_{\Delta t}^n}{(1 + \bar{n}_{\Delta t})^{n+1}} (\sin \Theta_n)^2, \quad (28)$$

where $\bar{n}_{\Delta t}$ is the average phonon number after heating over the duration Δt . We use delay times on the order of ms which is much larger than the duration of single-qubit gate operations which are on the order of 10 to 100 μs . Thus we neglect the heating during the gate operation. Here the bright population P_{\uparrow} is a direct measure of the final state fidelity and hence a good proxy metric for the single qubit gate fidelity. We repeat the same set of steps for multiple Δt values for each experimental set up of different beam arrangements, chain lengths, as well as axial frequencies.

Figure 1 shows the bright population P_{\uparrow} as a function of the average number of phonons \bar{n} , obtained according to the expression (28) for the axial frequency $2\pi \times 153\text{kHz}$. Specifically, we optimize P_{\uparrow} in (28) with respect to Ω_0 , while assuming the initial average phonon number is $\bar{n}_0 \approx 64$, whose value is commensurate to the Doppler limit of the axial mode. Once the specific Ω_0 is obtained, hereafter referred to as the static Rabi rate Ω_0^{st} , we may plot P_{\uparrow} as a function of \bar{n} . To compare, experimentally, we measure P_{\uparrow} as a function of the delay time Δt using the static Rabi rate Ω_0^{st} , calibrated without

any delay, and we map Δt to \bar{n} according to a constant heating rate model, i.e., $\bar{n} = \bar{n}_0 + \dot{\bar{n}}\Delta t$. The experiments were conducted on a single ion confined in a harmonic well, where the axial frequency was adjusted to $2\pi \times 153\text{kHz}$ by changing the voltages of the DC electrodes of the ion trap. The co-propagating beam set up was used with beam waists $w_x^f = 1.4\ \mu\text{m}$. In Fig. 1, we use $\dot{\bar{n}} \approx 96/\text{ms}$, which agrees with our model the best. The agreement in P_{\uparrow} decay between our static Rabi rate based model and experimental results confirms the effect of heating in the axial mode on the quantum gate fidelity.

B. Improvement in the quantum gate fidelity

Improvement in the the bright population P_{\uparrow} hence the quantum gate fidelity over the static approach may readily be achieved by the following. Recall in our static approach we assumed the Rabi rate to be that obtained for the average initial phonon number \bar{n}_0 . In theory, the bright population P_{\uparrow} may be maximized with respect to Ω_0 for any \bar{n} . If we thus allow for P_{\uparrow} to be individually optimized for different values of \bar{n} , we can obtain P_{\uparrow} values that are larger than those obtained by the static approach. Figure 1 shows the optimized P_{\uparrow} as a function of \bar{n} , which may be compared with the static counterpart. The experimental results are accordingly obtained by optimizing over the Rabi rate for each delay time Δt , mapped to \bar{n} as described previously with the same heating rate $\dot{\bar{n}}$ and initial average phonon number \bar{n}_0 . By adjusting the Rabi rate according to \bar{n} , we achieve improvement in the quantum gate fidelity. The optimal Rabi rate obtained from this approach is hereafter denoted as Ω_0^{opt} . Figure 1 (b) shows the agreement of the ratio $\Omega_0^{\text{opt}}/\Omega_0^{\text{st}}$ between experimental and simulated results. It is then possible, given a known initial temperature and heating rate, to predict the optimal Rabi rate for any quantum gate operation embedded in a quantum circuit without explicit calibration, thus improve the overall fidelity of the quantum circuit.

Further improvement in the quantum gate fidelity over the axial mode heating may be achieved by raising the axial mode frequency through the following two mechanisms. Firstly, increasing the mode frequency ω_A decreases η in (22), which in turn reduces the widths of the distribution of Θ_n with respect to a specific distribution of n and lessens its decoherence effect on the quantum gate operation. Figure 2 shows P_{\uparrow} as a function of \bar{n} for a variety of axial mode frequencies, ranging from $2\pi \times 153\text{kHz}$ to $2\pi \times 513\text{kHz}$. We observe that both the static and optimized P_{\uparrow} values decay slower in \bar{n} for higher frequencies. For a given \bar{n} , a factor R increase in the axial mode frequency approximately translates to the gate infidelity reduction by R , which is due to the fact that $1 - P_{\uparrow}$ is proportional to η^2 to the zeroth order. Secondly, increasing an axial mode frequency in most cases decreases the heating rate associated with the mode [26] thus improves the overall fidelity of any quantum circuit of depth larger

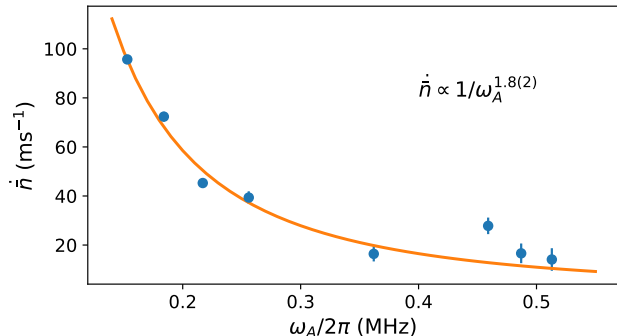


FIG. 3. Extracted heating rates \dot{n} for the axial mode of a single ion for eight different axial frequencies are shown as the blue circles. The orange solid line is the best fitted function of the form $\dot{n} = c/\omega_A^\alpha$.

than one.

C. Heating rate probe

We note that our model can in fact serve as a convenient tool in experiments to extract the heating rate of the axial mode for a single ion or for an ion chain if its COM mode heats much faster than the rest of the modes. To obtain an accurate estimate, the static and optimized P_\uparrow should be measured at different delay time Δt along with the optimal Rabi rate Ω_0^{opt} . We can then fit the experimental P_\uparrow as well as the ratio $\Omega_0^{\text{opt}}/\Omega_0^{\text{st}}$ to the theoretical predictions by adjusting the initial temperature \bar{n}_0 and the heating rate \dot{n} as fitting parameters. In our case, we fix the initial temperature \bar{n}_0 to the corresponding Doppler limit to reduce the number of fitting parameters. To account for all other mechanisms of decoherence that do not depend on the motional temperature but results in a reduction in P_\uparrow , we include an additional fitting parameter δP_\uparrow so that the final form of the fitting functions are given by

$$\begin{aligned}
 P_\uparrow^{\text{Exp}}(\Delta t) &\iff P_\uparrow^{\text{Sim}}(\bar{n}_0 + \dot{n}\Delta t) - \delta P_\uparrow, \\
 \Omega_0^{\text{opt,Exp}}(\Delta t) &\iff \Omega_0^{\text{opt,Sim}}(\bar{n}_0 + \dot{n}\Delta t), \\
 \Omega_0^{\text{st,Exp}} &\iff \Omega_0^{\text{st,Sim}} = \Omega_0^{\text{opt,Sim}}(\bar{n}_0). \quad (29)
 \end{aligned}$$

We put this method to test by repeating the same experiment on a single ion with axial mode frequency ω_A adjusted to several higher values from $2\pi \times 184$ kHz up to $2\pi \times 513$ kHz. Using the fitting method described above, we extract \dot{n} as a function of the axial mode frequency, shown in Fig. 3. We fit the heating rate to an inverse power law of the mode frequency and obtain $\dot{n} \propto \omega_A^{-1.8(2)}$.

Our method of measuring mode temperature for a single ion complements the method using sideband spectroscopy, in the way that, while sideband spectroscopy works for modes with mode vector projection along the

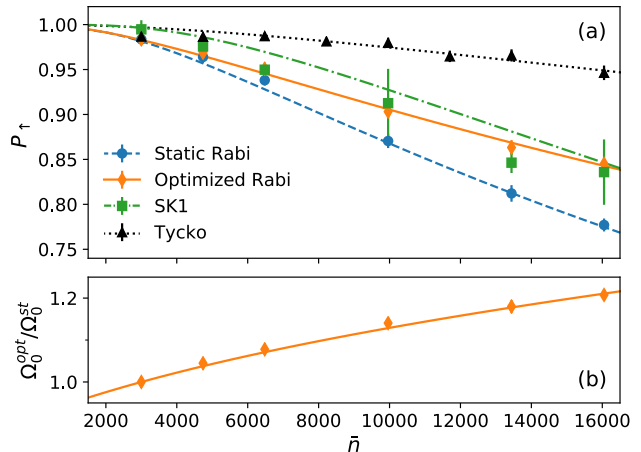


FIG. 4. Axial-heating error mitigation by compensating pulse sequences. We implement the delayed gate protocol (A)-(D) detailed in main text, while also using the SK1 and the Tycko three-pulse sequences. A 25-ion chain with the axial COM mode frequency $\omega_A = 2\pi \times 148$ kHz was used in a counter-propagating set up. (a) P_\uparrow as a function of \bar{n} . Experimental (points) and simulation (lines) results show the Tycko three-pulse (black triangles and dotted line) and SK1 (green squares and dash-dot line) compensating sequences effectively mitigate the P_\uparrow decay induced by the mode heating, observed by their better performance over the optimized (orange diamonds and solid line) and static (blue circles and dashed line) Rabi approaches without the compensating sequences. The simulation results for the SK1 or the Tycko three-pulse sequences assume a systematic phase error of 0.4 radian per gate. (b) the ratio $\Omega_0^{\text{opt}}/\Omega_0^{\text{st}}$ as a function of \bar{n} . The orange diamonds are the experimental results and the orange solid line is the theoretical simulation results.

beam propagation direction, our method works for mode with mode vector projection perpendicular to the beam propagation direction. We further note that, while the examples we show are for relatively large phonon numbers, it is straightforward to extend our method to lower phonon numbers. This may be achieved by reducing state-preparation and measurement error and single qubit gate error, as well as increasing η through reducing the effective beam waist w_x^{eff} . Narrow band composite pulse sequences that amplify amplitude errors in the qubit space can also be employed to increase the sensitivity of P_\uparrow to the heating rate. Note for an ion chain with more than one ion, the sensitivity is reduced due to the fact that η is generally proportional to $1/\sqrt{N}$.

D. Compensating pulse sequences

The error induced by excessive temperature of an axial thermal mode is in essence an amplitude error in the quantum gate unitary, which can be mitigated by composite pulse sequencing techniques [10, 11] that are

designed to target amplitude errors. In this section, we experimentally demonstrate the efficacy of the well-known SK1 pulse sequence and the Tycko three-pulse sequence [10, 27] (see below for detail) in mitigating the axial-temperature driven error. Specifically, we measure the bright populations P_{\uparrow} as a function of \bar{n} as done previously, along with simulations.

A single-qubit gate $\mathcal{R}(\theta, \phi)$ that rotates a Bloch vector by θ about the rotation axis on the equator of the Bloch sphere with polar angle ϕ may be parametrized as

$$\mathcal{R}(\theta, \phi) = \begin{pmatrix} \cos \frac{\theta}{2} & -ie^{-i\phi} \sin \frac{\theta}{2} \\ -ie^{i\phi} \sin \frac{\theta}{2} & \cos \frac{\theta}{2} \end{pmatrix}. \quad (30)$$

Then, the SK1 pulse sequence $\mathcal{R}_{\text{SK1}}(\pi, 0)$ is given by

$$\mathcal{R}_{\text{SK1}}(\pi, 0) = \mathcal{R}(2\pi, -\psi)\mathcal{R}(2\pi, \psi)\mathcal{R}(\pi, 0), \quad (31)$$

where $\psi = \arccos(-1/4)$. The Tycko three-pulse sequence $\mathcal{R}_{\text{Tycko}}(\pi, 0)$ is given by

$$\mathcal{R}_{\text{Tycko}}(\pi, 0) = \mathcal{R}(\pi, 2\pi/3)\mathcal{R}(\pi, 4\pi/3)\mathcal{R}(\pi, 2\pi/3). \quad (32)$$

In practice, we implement $\mathcal{R}(2\pi, \psi)$ in (31) by executing $\mathcal{R}(\pi, \psi)$ twice, and similarly for $\mathcal{R}(2\pi, -\psi)$.

Figure 4 shows the bright population P_{\uparrow} as a function of \bar{n} for the static and optimized Rabi rates, in addition to the SK1 and the Tycko three-pulse sequences introduced above. For the sequence-based approaches, we used the optimal Rabi rate Ω_0^{opt} approach detailed in Sec. V B. The experiment here was performed on the middle ion of a 25-ion chain which has a COM mode with a mode frequency $\omega_A = 2\pi \times 148$ kHz that heats the fastest. A counter-propagating set up is used where the individually addressing narrowly focused beam has a waist of $0.87(2) \mu\text{m}$ along the x -axis, while the globally addressing beam has a waist of $\sim 200 \mu\text{m}$. Sideband cooling of the horizontal modes is implemented before state preparation.

From Fig. 4, it is evident that these pulse sequences provide further improvement in quantum gate fidelity compared to the optimized Rabi approach, with the Tycko three-pulse sequence especially standing out. Note to reach the agreement between the experimental data and the simulation result for the pulse sequences, we assumed a progressively increasing phase error of 0.4 radian per gate that can be attributed to miscalibrated light shift as well as the qubit frequency error. Such a phase error has no effect on the P_{\uparrow} of a single Rabi pulse, but reduces the efficacy of the composite pulse sequences. A better calibrated single qubit gate as the basis gate that composes the SK1 or the Tycko three-pulse sequences will improve the P_{\uparrow} even further.

VI. DISCUSSION

In this paper, we have investigated the effect of non-idealities in ion-beam geometry in quantum gate fidelity.

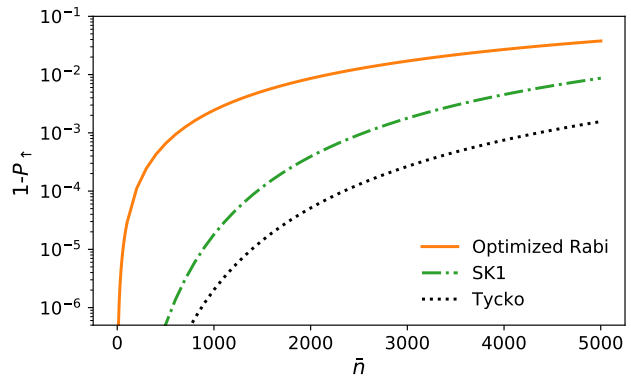


FIG. 5. Theoretical simulation of the infidelity of the final state, represented by $1 - P_{\uparrow}$, of the middle ion in a 25-ion chain as a function of \bar{n} . Only the decoherence effect of the axial COM mode with a frequency of $2\pi \times 148$ kHz is considered. The orange solid line represents the optimized Rabi approach, the green dash-dotted line represents the SK1 pulse sequence case, and the black dotted line represents the Tycko three-pulse sequence case.

Specifically, we have provided a general theoretical framework that can be used to systematically examine the effect of the coupling between the external degrees of freedom of the ion-light field system and the qubit space on quantum gate operations to any desirable accuracy. As a concrete, explicit example, we performed a comprehensive analysis focused on the effect of excessive axial-mode temperature and confirmed our model's validity by comparison with experiments. Guided by our model, we successfully mitigated the effect and increased our quantum gate fidelity.

To further improve, we suggest the following. From our model, it is straightforward to show that the gate fidelity improves rapidly when decreasing the temperature (see Fig. 5). Therefore, from the hardware design point of view, reducing heating rate of a trap itself a modest amount would help dramatically. We can also consider efficient sympathetic cooling scheme during a quantum circuit execution as well [28, 29], keeping \bar{n} to an acceptable level throughout the quantum computational runtime. Raising axial mode frequencies by either decreasing the ion spacing or using optical tweezers [30] is also a viable way to improve quantum gate fidelity, since this helps reduce the size of η and may reduce the heating rate. We further note that increasing the waist of the individually addressing beam will directly decrease η , thus reducing the undesirable decoherence. Finally, composite pulse sequences, as we have demonstrated, can significantly improve fidelity. Figure 5 shows additional simulation data that shows the expected infidelity $1 - P_{\uparrow}$ for the SK1 and the Tycko three-pulse sequences. It is clear that the composite pulse sequences can significantly increase the range of \bar{n} acceptable for a successful quantum gate operation with high fidelity.

Looking forward, building on our exercise, additional terms in the interaction Hamiltonian can now be systematically included in descending order of their contribution towards quantum gate infidelity to help achieve high fidelity trapped-ion quantum computing. For example, we can include the Debye-Waller effect inducing terms B_0^\pm . We can consider higher order terms in the B_1^\pm function as well that originated from the Gouy phase. Note the latter will manifest themselves as a small correction to the Debye-Waller effect. These terms will induce decoherence, if the temperature of the motional modes of an ion chain is high and/or the misalignment between the ion and its addressing beam is large. Our framework analytically captures these effects accurately and provides quantitative methodologies to characterize their impact on quantum gate fidelity.

Although we have largely focused on the effect on single-qubit gate operations in our analysis and experiments, pertaining the coupling to the axial modes, similar derivation and analysis can readily be extended to two-qubit gates. In fact, most of the conclusion including mitigation strategies and techniques for single-qubit gates hold analogous and similar counterparts for two-qubit gates.

VII. CONCLUSION

In this paper, we have derived a general Hamiltonian capable of pinpointing the sources of infidelity in trapped-ion quantum computers with a long chain. By carefully analyzing the Hamiltonian with realistic beam geometry and parameters, quantum computational errors incurred due to alignment and focus have been identified and experiments were conducted to confirm their existence. Our framework is versatile, precisely laying out all terms of importance according to the quality requirement for any trapped-ion quantum computing platform. We expect our results will help guide the quantum hardware engineers to make informed decisions, tailored for future hardware design criteria.

VIII. ACKNOWLEDGEMENT

The authors would like to thank Shantanu Debnath and Kevin Landsman for their contribution in designing and implementing experimental system components and Christopher Monroe, Jungsang Kim, and Marco Cetina for helpful discussions.

-
- [1] J. P. Gaebler, T. R. Tan, Y. Lin, Y. Wan, R. Bowler, A. C. Keith, S. Glancy, K. Coakley, E. Knill, D. Leibfried, and D. J. Wineland, *Phys. Rev. Lett.* **117**, 060505 (2016).
- [2] C. J. Ballance, T. P. Harty, N. M. Linke, M. A. Sepiol, and D. M. Lucas, *Phys. Rev. Lett.* **117**, 060504 (2016).
- [3] D. Kielpinski, C. Monroe, and D. J. Wineland, *Nature* **417**, 709 (2002).
- [4] J. M. Pino, J. Dreiling, C. Figgatt, J. Gaebler, S. Moses, M. S. Allman, C. Baldwin, M. Foss-Feig, D. Hayes, K. Mayer, C. Ryan-Anderson, and B. Neyenhuis, arXiv preprint arXiv:2003.01293 (2020).
- [5] C. Monroe, R. Raussendorf, A. Ruthven, K. R. Brown, P. Maunz, L.-M. Duan, and J. Kim, *Phys. Rev. A* **89**, 022317 (2014).
- [6] N. M. Linke, D. Maslov, M. Roetteler, S. Debnath, C. Figgatt, K. A. Landsman, K. Wright, and C. Monroe, *Proceedings of the National Academy of Sciences* **114**, 3305–3310 (2017).
- [7] Y. Nam and D. Maslov, *npj Quantum Information* **5** (2019), 10.1038/s41534-019-0152-0.
- [8] D. Maslov, Y. Nam, and J. Kim, *Proceedings of the IEEE* **107**, 5 (2019).
- [9] N. Grzesiak, R. Blümel, K. Wright, K. M. Beck, N. C. Pisenti, M. Li, V. Chaplin, J. M. Amini, S. Debnath, J.-S. Chen, and et al., *Nature Communications* **11** (2020), 10.1038/s41467-020-16790-9.
- [10] L. M. K. Vandersypen and I. L. Chuang, *Rev. Mod. Phys.* **76**, 1037 (2005).
- [11] J. T. Merrill and K. R. Brown, “Progress in compensating pulse sequences for quantum computation,” in *Quantum Information and Computation for Chemistry* (John Wiley & Sons, Ltd, 2014) pp. 241–294.
- [12] M. Cetina, L. Egan, C. A. Noel, M. L. Goldman, A. R. Risinger, D. Zhu, D. Biswas, and C. Monroe, arXiv preprint arXiv:2007.06768 (2020).
- [13] A. West, R. Putnam, W. Campbell, and P. Hamilton, arXiv preprint arXiv:2007.10437 (2020).
- [14] E. Brion, L. H. Pedersen, and K. Mølmer, *Journal of Physics A: Mathematical and Theoretical* **40**, 1033 (2007).
- [15] D. F. V. James, *Applied Physics B* **66**, 181 (1998).
- [16] A. E. Siegman, *Lasers* (University Science Books, Mill Valley, Calif., 1986).
- [17] K. Mølmer and A. Sørensen, *Phys. Rev. Lett.* **82**, 1835 (1999).
- [18] A. Sørensen and K. Mølmer, *Phys. Rev. Lett.* **82**, 1971 (1999).
- [19] J. I. Cirac and P. Zoller, *Phys. Rev. Lett.* **74**, 4091 (1995).
- [20] D. J. Wineland, C. Monroe, W. M. Itano, D. Leibfried, B. E. King, and D. M. Meekhof, *J. Res. Natl. Inst. Stand. Technol.* **103**, 259 (1998).
- [21] R. Blümel, N. Grzesiak, and Y. S. Nam, ArXiv preprint arXiv:1905.09292 (2019).
- [22] For sideband cooled horizontal modes in counter-propagating set up, see discussion on Debye-Waller effect in Sec. IV B.
- [23] Note that the terms with odd l in Eq. (21) are suppressed by the alignment parameter ξ due to the fact that the zeroth order terms of the odd Hermite polynomials are on the order of ξ instead of a constant. Therefore, the coefficients in front of the imbalanced terms are one ξ order smaller than the balanced terms.
- [24] K. Wright, K. M. Beck, S. Debnath, J. M. Amini, Y. Nam, N. Grzesiak, J.-S. Chen, N. C. Pisenti, M. Chmielewski, C. Collins, K. M. Hudek, J. Mizrahi,

- J. D. Wong-Campos, S. Allen, J. Apisdorf, P. Solomon, M. Williams, A. M. Ducore, A. Blinov, S. M. Kreike-meier, V. Chaplin, M. Keesan, C. Monroe, and J. Kim, Nature Communications **10**, 5464 (2019).
- [25] S. Olmschenk, K. C. Younge, D. L. Moehring, D. N. Matsukevich, P. Maunz, and C. Monroe, Phys. Rev. A **76**, 052314 (2007).
- [26] I. A. Boldin, A. Kraft, and C. Wunderlich, Phys. Rev. Lett. **120**, 023201 (2018).
- [27] R. Tycko, Phys. Rev. Lett. **51**, 775 (1983).
- [28] M. D. Barrett, B. DeMarco, T. Schaetz, V. Meyer, D. Leibfried, J. Britton, J. Chiaverini, W. M. Itano, B. Jelenković, J. D. Jost, C. Langer, T. Rosenband, and D. J. Wineland, Phys. Rev. A **68**, 042302 (2003).
- [29] J. P. Home, D. Hanneke, J. D. Jost, J. M. Amini, D. Leibfried, and D. J.

- Wineland, Science **325**, 1227 (2009), <https://science.sciencemag.org/content/325/5945/1227.full.pdf>.
- [30] Y.-C. Shen and G.-D. Lin, New Journal of Physics **22**, 053032 (2020).

Appendix A: Up to the second order expansion in \hat{p}_1

Inspecting the A and B functions in (15), we notice that B_0^\pm are already in the form of a simple power series of \hat{p}_1 . For the rest, we transform the summations in (15) over n and, if necessary, m into functions in compact forms with respect to the zeroth, first, and second order terms of \hat{p}_1 . All orders in \hat{q}_1 are kept. To simplify the expressions, we define $s_0 = 1/\sqrt{1+p_0^2}$ and $\hat{s}_\pm = s_0\sqrt{\pm i(p_0 + \hat{p}_1)}$. We then have

$$\begin{aligned}
A_1 &= s_0^{1/2} \left[1 - \frac{p_0}{2} s_0^2 \hat{p}_1 + \frac{3p_0^2 - 2}{8} s_0^4 \hat{p}_1^2 + \mathcal{O}(\hat{p}_1^3) \right], \\
A_2 &= \sum_{l_q=0}^{\infty} (s_0 \hat{q}_1)^{l_q} \sum_{n=\lceil l_q/2 \rceil}^{\infty} \frac{(-1)^n}{n!} \binom{2n}{l_q} (s_0 q_0)^{2n-l_q} [1 - 2n s_0^2 p_0 \hat{p}_1 + \{(2n^2 + n)p_0^2 - n\} s_0^4 \hat{p}_1^2 + \mathcal{O}(\hat{p}_1^3)] \\
&= e^{-s_0^2 q_0^2} \sum_{l_q=0}^{\infty} \frac{(-s_0 \hat{q}_1)^{l_q}}{l_q!} \left[\mathcal{H}_{l_q}(s_0 q_0) - s_0^2 p_0 \{l_q \mathcal{H}_{l_q}(s_0 q_0) - s_0 q_0 \mathcal{H}_{l_q+1}(s_0 q_0)\} \hat{p}_1 + \right. \\
&\quad \left. s_0^4 \left\{ \left[\frac{p_0^2}{2} (l_q - 2s_0^2 q_0^2)(l_q + 1) - \frac{l_q}{2} \right] \mathcal{H}_{l_q}(s_0 q_0) + \left[p_0^2 s_0 q_0 (s_0^2 q_0^2 - l_q - 1) + \frac{s_0 q_0}{2} \right] \mathcal{H}_{l_q+1}(s_0 q_0) \right\} \hat{p}_1^2 + \mathcal{O}(\hat{p}_1^3) \right], \\
B_1^\pm &= e^{\pm \frac{i}{2} \arctan(p_0)} \left[1 + \frac{\pm i}{2} s_0^2 \hat{p}_1 - \frac{1 \pm 4ip_0}{8} s_0^4 \hat{p}_1^2 + \mathcal{O}(\hat{p}_1^3) \right], \\
B_2^\pm &= \sum_{l_q=0}^{\infty} (s_0 \hat{q}_1 \sqrt{p_0 + \hat{p}_1})^{l_q} \sum_{n=\lceil l_q/2 \rceil}^{\infty} \frac{(\mp i)^n}{n!} \binom{2n}{l_q} (s_0 q_0 \sqrt{p_0 + \hat{p}_1})^{2n-l_q} [1 - 2n s_0^2 p_0 \hat{p}_1 + \{(2n^2 + n)p_0^2 - n\} s_0^4 \hat{p}_1^2 + \mathcal{O}(\hat{p}_1^3)] \\
&= e^{\mp i s_0^2 q_0^2 p_0} B_0^\pm (s_0^2 q_0^2 \hat{p}_1) \sum_{l_q=0}^{\infty} \frac{(-\hat{s}_\pm \hat{q}_1)^{l_q}}{l_q!} \left[\mathcal{H}_{l_q}(\hat{s}_\pm q_0) - s_0^2 p_0 \{l_q \mathcal{H}_{l_q}(\hat{s}_\pm q_0) - \hat{s}_\pm q_0 \mathcal{H}_{l_q+1}(\hat{s}_\pm q_0)\} \hat{p}_1 + \right. \\
&\quad \left. s_0^4 \left\{ \left[\frac{p_0^2}{2} (l_q - 2\hat{s}_\pm^2 q_0^2)(l_q + 1) - \frac{l_q}{2} \right] \mathcal{H}_{l_q}(\hat{s}_\pm q_0) + \left[p_0^2 \hat{s}_\pm q_0 (\hat{s}_\pm^2 q_0^2 - l_q - 1) + \frac{\hat{s}_\pm q_0}{2} \right] \mathcal{H}_{l_q+1}(\hat{s}_\pm q_0) \right\} \hat{p}_1^2 + \mathcal{O}(\hat{p}_1^3) \right], \tag{A1}
\end{aligned}$$

where $\mathcal{H}_n(x)$ denotes the n th-order Hermite polynomial. The B_2^\pm functions are the most complicated, expanded in a power series of $\hat{s}_\pm \hat{q}_1$. Despite the square root in the operator \hat{s}_\pm , the total power on each \hat{s}_\pm term is guaranteed to be an even number, which removes the square root

and only leaves integer powers of the ladder operators. Note that for a specific sum index l_q , the lowest power of \hat{q}_1 that appear in the summand of B_2^\pm is l_q . Similarly, for a specific l_q , the lowest power of \hat{p}_1 that appear in the same summand is $2\lceil l_q/2 \rceil$.